Topology of ON and OFF inputs in visual cortex enables an invariant columnar architecture

Kuo-Sheng Lee[1,2], **Xiaoying Huang**[1], and **David Fitzpatrick**[1]

[1]Department of Functional Architecture and Development of Cerebral Cortex, Max Planck Florida Institute for Neuroscience, Jupiter, FL, USA

[2]Integrative Biology and Neuroscience Graduate Program, Florida Atlantic University, Boca Raton, FL, USA

Abstract

Circuits in visual cortex integrate the information derived from separate ON and OFF pathways to construct orderly columnar representations of orientation and visual space[1–7]. How this transformation is achieved to meet the specific topographic constraints of each representation remains unclear. Here we report several novel features of ON/OFF convergence visualized by mapping the receptive fields of layer 2/3 neurons in tree shrew visual cortex using two-photon imaging of GCaMP6 calcium signals. The spatially separate ON and OFF subfields of simple cells in layer 2/3 were found to exhibit topologically distinct relationships with the maps of visual space and orientation preference. The centers of OFF subfields for neurons in a given region of cortex were confined to a compact region of visual space and displayed a smooth visuotopic progression. In contrast, the centers of the ON subfields were distributed over a wider region of visual space, displayed significant visuotopic scatter, and an orientation-specific displacement consistent with orientation preference map structure. As a result, cortical columns exhibit an invariant aggregate receptive field structure: an OFF-dominated central region flanked by ON-dominated subfields. This distinct arrangement of ON- and OFF- inputs enables continuity in the mapping of both orientation and visual space and the generation of a columnar map of absolute spatial phase.

Circuits in visual cortex transform the inputs supplied by ON- and OFF-center lateral geniculate axons into a columnar architecture that preserves the orderly mapping of visual space, while generating *de novo* an iterated map of stimulus orientation[1–5]. The first step in this process involves the convergence of ON and OFF inputs onto single cortical neurons creating 'simple' receptive fields that exhibit spatially offset ON and OFF subfields[1,6,7]. Understanding the logic that cortical circuits use to integrate the ON and OFF pathways in

order to build this columnar architecture requires the ability to visualize the receptive fields of large numbers of simple cells, determine the spatial arrangement of their ON and OFF subfields, and how this relates to the columnar maps of orientation and visual space. We have achieved this by using two-photon calcium imaging to map the receptive fields of large numbers of single neurons in layer 2/3 of the tree shrew, a species with a close phylogenetic relation to primates[8], and a visual cortex with a well-developed columnar architecture[5,9–11].

Previous studies in tree shrew have shown that ON and OFF- LGN inputs target separate populations of neurons in cortical layer 4, and that the projections from layer 4 to layer 2/3 bring about the convergence of ON and OFF inputs onto single layer 2/3 neurons[12,13]. Here we mapped the receptive fields of single layer 2/3 neurons with reverse correlation to a sparse noise visual stimulus and analyzed the spatial distribution of ON and OFF responses[14] (Extended Data Fig. 1, all statistical details can be found in Supplementary Notes). Layer 2/3 neurons exhibited robust responses to the sparse noise stimulus making it possible to reliably reconstruct the receptive fields of hundreds of single layer 2/3 neurons per region of interest (generally 0.36–1.0 mm^2) (Fig. 1a, b) A large fraction (42%) of the layer 2/3 neurons that exhibited significant receptive fields with this stimulus had spatially offset ON and OFF subfields, consistent with the organization of simple cells that has been described in other species. Other layer 2/3 neurons exhibited single sign receptive fields (16% ON, 33% OFF) and a relatively small percentage appeared to have complex receptive fields with overlapping ON and OFF responses (9%) (Extended Data Fig. 2).

As a first step in understanding the transform that underlies cortical columnar architecture, we examined the distribution in visual space of the receptive fields and the ON and OFF subfields of the simple cells that were found in a 1 mm^2 field of view. The receptive field centers of the neurons in the field of view were displaced over about 5 degrees of visual space, a distance consistent with previous studies of the mapping of visual space in this species (average cortical magnification factor 0.2 mm/degree[5,10]). The centers of the ON and OFF subfields, however, exhibited a strikingly different distribution in visual space (Fig. 1c): the centers of the OFF subfields were clustered within a compact region of visual space; while the ON subfield centers were spread over a greater region of visual space, distributed around the region occupied by the OFF subfield centers. To quantify this difference, we computed the ratio of mean pairwise distances within each group, and compared this with the results found after shuffling polarity identity (Fig. 1d). These results reveal a fundamental difference in the visuotopic mapping of ON and OFF inputs in layer 2/3: the ON inputs that contribute to neural responses in a given region of the cortex originate from a broader region of visual space than the OFF inputs. Epi-fluorescence imaging of population responses produces patterns of cortical activation that are consistent with these observations: a significantly greater area of the cortical surface is activated following stimulation by a light bar compared to a dark bar of the same size (Extended Data Fig. 3).

Next we evaluated the precision of the visuotopic mapping of the receptive fields and the ON and OFF subfields for the neurons with simple receptive fields in a given region of visual cortex. The receptive field centers of the neurons In a 1 mm^2 field of view always exhibited a clear progression in both azimuth and elevation. The centers of the OFF subfields also exhibited systematic progressions in both dimensions, and these were even

more regular than what was observed for receptive field centers. In contrast, the ON subfields from the same population exhibited a striking degree of disorder: adjacent neurons frequently had receptive fields with quite different ON subfield center locations and there was little sign of fine visuotopic progression (Fig. 2a–c). Similar results were found for all eight sampled cortical regions for both simple (Fig. 2d–e) and single sign cells (Extended Data Fig. 4). The visuotopic progression of OFF subfields is consistent with that predicted for a smooth visuotopic map with a deviation less than 1 degree, while the pattern of ON subfields cannot be explained by a smooth visuotopic progression. We conclude that the OFF inputs to layer 2/3 neurons are arranged with fine visuotopic precision that is absent for ON inputs.

In most simple cells in other species, the visuotopic displacement of the ON and OFF subfields is correlated with the cell's orientation preference: subfields are displaced along an axis in visual space that is orthogonal to the cell's preferred orientation[1,4,15–17]. This suggests that the disorderly visuotopic arrangement of ON subfields in layer 2/3 neurons might be explained by their orderly arrangement in relation to the map of orientation preference. To test this possibility, we first compared the preferred orientation of individual neurons to that predicted by the axis of displacement of the ON and OFF center subfields and verified this strong correlation at the level of single neurons (Fig. 3a). Next we asked how well the visuotopic locations of the ON subfield centers of the neurons in a column (within 80 μm diameter region, orientation difference within 11.25° from the mean, see Methods) predicted the preferred orientation of the column. The locations of the ON subfield centers for the simple cells in a column are highly clustered in visual space forming dipoles that strongly predict the orientation preference of the column (Fig. 3b, c). Thus both the ON and OFF pathways exhibit a high degree of precision in their topological arrangement but for different columnar maps: the OFF pathway exhibits precision for the map of visual space while the ON pathway exhibits precision for the map of orientation preference. The distinct topological arrangement of both ON and OFF subfield centers that we have demonstrated for individual columns is maintained at the single neuron level, irrespective of location in the orientation map. (Extended Data Fig. 5).

These observations suggest that all orientation columns have simple cells that are arranged with a fundamentally similar visuotopic structure: an OFF-dominated central region flanked by ON-dominated subfields. To test this possibility we computed the aggregate receptive field (ARF) for a cortical column, simply overlaying the ON and OFF subfields for each neuron in the column based on their position in visual space (Extended Data Fig. 6). Individual neurons in the column exhibit different subfield organization with an average of 2–3 subfields. Overlaying all the simple cell RFs in the column results in a column aggregate receptive field that is somewhat larger than the receptive fields of the individual neurons in the column, but clearly exhibits an OFF dominated central region flanked by two ON-dominated regions. In essence, the aggregate receptive field of a column resembles an OFF-centered simple cell receptive field and it can be well fit by a 2D Gabor function[14,16,17] (Fig. 3d). Similar results were found for all other columns in our sample (N=73). Fits to the 2D Gabor function show the similarity across columns in the relative phase of the aggregate subfields, number of half-cycles, and aspect ratio (Fig. 3e), and these fits accurately predict the column's preferred orientation and visuotopic location (Fig. 3f). The spatial frequency

preference measured with grating stimuli was systematically underestimated by the linear receptive field analysis, consistent with previous observations from electrophysiological recordings[15].

The fact that OFF inputs serve as the anchor for the aggregate receptive fields of cortical columns and that OFF inputs exhibit a precise visuotopic organization predicts that preference for absolute spatial phase—the phase of a sine wave grating stimulus measured relative to a common reference point in visual space--should also be mapped in a smooth and continuous fashion in the responses of layer 2/3 neurons. To test this prediction, we examined cortical responses of large populations of single neurons while presenting an elongated two-period grating with different phases relative to the center location of the population receptive field (see Methods). This stimulus reveals a strong absolute spatial phase preference in the majority of layer 2/3 neurons (83.7 % tuned; mean tuning bandwidth ± s.d.: 16.9 ± 5.55 degree) and an orderly progression across the cortical surface (Fig. 4a, b). The phase tuning curve for the neurons can be well described by circular Gaussian curve fitting and is consistent with the receptive field structure of the neurons (Extended Data Fig. 7a–b). The absolute spatial phase parameter of the Gabor fit to the ARF accurately predicts the preferred phase of the column (Extended Data Fig. 7c). For a given region of cortex, we found that the preferred phase is comparable at multiple depths, consistent with a columnar organization (Extended Data Fig. 7d–e).

The systematic mapping of preferred absolute spatial phase is especially evident at the larger spatial scales accessible with wide field epi-fluorescence imaging (Fig. 4c.). In these images, the spread of the fluorescent signals beyond the cell bodies of stimulated orientation columns (due to calcium signals in the neuropil as well as light scattering), emphasizes the linear progression of the phase map along the axis of visual space orthogonal to the stimulus orientation. The linear fit to the experimental data for each 360° periodic phase cycle accounts for the organization of the absolute spatial phase preference map (Fig. 4d.) and the intersection angle between the gradient of the maps for visuotopy and absolute spatial phase shows that they are parallel to each other (Fig. 4e; Extended Data Fig. 7f–g). Moreover, our analysis indicates that complete coverage for phase and orientation is present within the cortical area corresponding to one degree of visual space, and that uniformity of coverage increases with the amount of visual space included (Extended Data Fig. 8).

The striking differences in the topology of ON and OFF inputs to layer 2/3 simple cells is reminiscent of the structural and functional differences that have been described for ON- and OFF- center retinal ganglion cells in a number of species[18–20]. Compared to ON-center ganglion cells, OFF-center ganglion cells are more numerous and have smaller dendritic fields, endowing them with a capacity for greater spatial resolution that accords with natural scenes statistics showing more regions of negative vs positive contrast[20]. Previous computational[21,22] and experimental studies[3,4] have recognized that the spatial arrangement of ON- and OFF- center inputs is likely to provide the scaffold for orientation column structure, but exactly how the ON and OFF pathways converge to generate coherent maps of orientation and visual space has remained unclear. Our results provide evidence that the retinal asymmetries in the ON and OFF pathways are reflected in cortical map structure such that simple cell receptive fields preserve a high degree of visuotopic order in their OFF

subfield inputs, while exploiting visuotopic displacement of their ON subfield inputs as a means for generating an orderly representation of orientation preference. In addition, the resulting OFF-anchored columnar architecture enables emergence of an additional orderly representation of absolute spatial phase—a property that contains a wealth of information about the visual scene that can be used to efficiently encode spatial patterns[23,24], motion[25], and depth[26]. We emphasize that the modular representation of absolute spatial phase preference demonstrated here is distinct from the modular representation of polarity preference that has been described in cat[3–4] and ferret layer 4, and more recently in ferret layer 2/3[27]. Despite species differences in the representation of polarity, electrophysiological studies in layer 4 of the cat visual cortex suggest that there are common rules governing the convergence of ON and OFF inputs to build orientation selective simple cells, and that the modular representation of absolute spatial phase is a general principle of cortical organization common to a broad range of species with well-developed columnar architecture[28]. Interestingly, despite the local diversity of orientation preference and receptive field structure in mouse visual cortex, adjacent neurons are found to exhibit specificity in the overlap of their ON and/or OFF subfields that is predictive of connectivity[29,30], consistent with the idea that the topology of ON and OFF inputs shapes the organization of cortical circuits even in the absence of cortical columns.

Methods

All experimental procedures were approved by the Max Planck Florida Institute for Neuroscience Animal Care and Use Committee and performed in compliance with guidelines published by the National Institutes of Health. Tree shrews (*Tupaia belangeri*, n = 18, 2–4 months of age, male and female) were injected with a virus expressing GCaMP6s[31], and then used in a terminal imaging experiment after a 10–15 day survival period. Animal numbers were minimized to conform to ethical guidelines while accurately measuring parameters of animal physiology.

Viral expression of GCaMP6s

Tree shrews were initially anesthetized with Midazolam (100 mg/kg, IM), Ketamine (100 mg/kg, IM) and given atropine (0.5 mg/kg, SC) to reduce secretions. A long acting analgesic (slow release Buprenorphine, 0.6 mg/kg, SC) was administered before the surgery. The animal's head was shaved, any remaining hair was removed with Nair, and the surgical site was injected with a mixture of bupivacaine and lidocaine (0.3–0.5 ml, SC). The mixture of oxygen and nitrous oxide (O_2/N_2O 1:0 to 1:2) and gas anesthesia (isoflurane 0.5–2%) were initially delivered through a mask and later shifting to intubation tube. Venous cannulation (tail or hind limb) and tracheal intubation were established after animal no longer responded to toe-pinching. Internal temperature (37–38 °C) was maintained by a thermostatically controlled heating pad while expired CO_2 and heart rate were monitored for any signs of stress. Artificial respiration was provided between 100–130 strokes per minute trough ventilator. The animal was placed in a stereotaxic device (Kopf, Model 900 Small Animal Stereotaxic Instrument), a small incision was made, skin and muscle were retracted, and a small craniotomy (about 1 mm diameter) was made over the center of primary visual cortex. Visual cortex was injected with 1–2 μl of virus solution (1 x 10^{13} GC/ml – 2x 10^{13} GC/ml)

containing AAV2/9-Syn-GCaMP6s.WPRE.SV40 (Penn Vector Core) through a beveled glass micropipette (tip size 10–20μm diameter, Drummond Scientific Company) using a nanoinjector (Drummond Nanoject II, WPI) at a depth of 200 and 400 μm from the cortical surface. Only one injection was placed in one hemisphere of each animal. After the injection, the craniotomy was covered with bone wax and the scalp incision was closed with 4-0 Ethilon sutures. Neosporin was applied to the wound margin. The animals were then placed on a heating blanket in a small cage to recover from anesthesia. A period of 10–15 days was allowed for expression time prior to two-photon imaging experiments. GCaMP6s expression was found in approximately $84 \pm 2.3\%$ of the neurons in the superficial part of layer 2/3 (within 500 μm of the surface, N = 4 animals). The densely labeled area was generally 5–7 mm in diameter.

Preparation for two-photon imaging experiments

After 10 to 15 days of expression, anesthesia was induced with Midazolam (100 mg/kg, IM), Ketamine (100 mg/kg and 0.2–0.5 mg/kg, IM) and atropine (0.5 mg/kg, SC) was delivered to reduce secretions. An analgesic (Buprenorphine, 0.3–0.6 mg/kg, SC) was administered before the surgery. Peripheral venous line on either tail or hind limbs and intubation were made for delivering fluid during surgery and muscle relaxants during imaging experiments. All regions identified as incisions sites for the surgery were treated with a mixture of bupivacaine and lidocaine (0.3–0.5 ml, SC), and ear bars were applied with Lidocaine ointment (5%). Gas anesthesia (isoflurane 0.5–2% in O_2/N_2O 1:0 to 1:2) was delivered via artificial respiration following intubation or tracheotomy. The animals' head was shaved and placed in a customized stereotaxic device that did not obstruct the view of the stimulus screen. Body temperature (37–38 °C) was maintained by a thermostatically controlled heating pad and expired CO_2 (3.5 –4.5%) and heart rate were monitored for any signs of stress. An incision about 2 cm was made over the skull near the midline, skin and muscle were retracted to the side. A head-plate with a central opening was attached to skull with dental cement (C & B Metabond) and a craniotomy (6 x 6 mm) was made centered over the injection site of GCaMP6s within primary visual cortex. After removing the dura mater, a piece of double-layer cover slip composed of a small round glass coverslip (3 mm diameter, 0.7 mm thickness, Warner Instruments) glued to a larger coverslip (8 mm diameter, 0.17 mm thickness, Electron Microscopy Sciences), with an optical adhesive (Norland Optical Adhensive 71) was placed onto the brain to gently compress the cortex and reduce biological motion during imaging. For some animals, a custom metal insert (5 mm diameter, 0.5 mm thickness for inner hole) attached with a coverslip (5 mm diameter, 0.17 mm thickness, Electron Microscopy Sciences) was used to achieve better optic transmission and larger field of view. The cover slip or metal insert was sealed with a snap ring (5/16″ internal retaining ring, McMaster-Carr) that fit into the chamber. Contact lenses were placed on both eyes for protection and stability. During imaging experiments, Isoflurane level was decreased to 0.5–1%. Pancuronium bromide or vecuronium bromide (2 mg/kg/hr, IV) was used as a paralytic to prevent eye movements.

Two-photon imaging experiments

Imaging experiments were performed using a B-Scope (Thorlabs) either with 910 nm excitation provided by an InSight DS+ (Spectra-Physics) or with 910 nm excitation provided

by a Mai Tai DeepSee laser (Spectra-Physics), running Scanimage 4.1 or 4.2 (Vidrio Technologies)[32]. Average excitation power at the exit of the objective (16x, CFI75, Nikon Instruments) ranged from 16 to 40 mW. Images were acquired at 15–30 Hz (512x512 pixels, field of view (FOV) ranges from 0.44x0.44 to 1.1x1.1 mm^2). Two-photon frame triggers from Scanimage and events denoting stimulus onset, stimulus offset, and stimulus identity were recorded using Spike2 (CED; Cambridge, UK). In a typical imaging session lasting about 16 hours, 2–4 different fields of view were sampled and at each site, data were acquired at 2–4 different depths with at least 35 microns separation, ranging from 50 and 350 microns below the cortical surface. Z-stacks of individual fields of view were acquired by averaging 50 frames per plane using 1μm steps from the surface to about 350 microns deep.

Epi-fluorescence imaging experiments

Epi-fluorescence imaging was performed using a custom light path on the B-Scope with 525 nm LED illumination (Thorlabs). GCaMP6s fluorescence signal from the cortical surface was acquired at about 15 Hz (640x540 pixels, field of view (FOV) ranges from 3x2.53 to 4x3.38 mm^2) using a Xyla sCMOS camera (Andor) controlled by μManager2. Average excitation power at the exit of the objective (4x, UPlanFl, Olympus) ranged from 0.2 to 0.8 mW. Epi-fluorescence frame triggers from μManager2 and stimulus events were recorded using Spike2 (CED; Cambridge, UK). The visual stimulus and the analysis method were the same as two-photon pixel based experimental design. Z-projections of two-photon fields of view were aligned to the epi-fluorescence imaging with the blood vessel pattern.

Visual stimulation

Visual stimuli were displayed on a LED monitor (29 cm x 51 cm, height x width) with a resolution of 1920 x 1080 pixels, which was placed in front of the center of the animal to cover about 100 degrees in azimuth and 70 degrees in elevation. The refresh rate of the monitor was 120 Hz, and the mean luminance for gray background was 54 cd/m^2. The stimulus monitor was placed at a distance of 21 cm from the eyes. Receptive fields of neurons in the field of view usually appeared close to the center of the monitor. Visual stimuli were generated using Psychopy2 written in Python. There were two main types of visual stimulation experiments: 1) sparse noise stimulus for mapping the receptive field[14], and 2) grating or bar stimulus for accessing tuning properties. Sparse noise stimuli were composed of two non-overlapped squares (2x2 grid size, separated within a 4 grid unit, with black or white sign presented independently) on a 17 by 17 square grid gray background (a total of 7904 images), which occupied 17 or 25 degrees of visual space. Individual images were presented for 200 ms without inter-stimulus interval. Depending on imaging quality, 1–2 trials of the entire stimulus set was presented, which lasted 26 to 52 minutes. For measuring orientation tuning properties, square wave gratings (contrast 100%, spatial frequency (SF) 0.25 cycles/°, and temporal frequency (TF) 4 Hz, stimulus duration 2 s, full screen) drifting in both directions were presented at 16 different orientations (0–168.75°, spaced at 11.25°). For measuring visuotopic position tuning, a single static bar (either black or white with 100% contrast, 6° by 24°, 1.5 s duration, centered on the population receptive field center) was presented at 8 different positions (0–21°, spaced with 3°). For measuring spatial frequency tuning, sine wave gratings (contrast 100%, preferred orientation for the

recording site, and temporal frequency 4 Hz, stimuli duration 2 s, full screen) drifting in both directions were presented at 8 different spatial frequencies (0.025 – 3.2 cycles/°, spaced at 1 unit in log2 scale). For measuring absolute spatial phase tuning, static sine wave gratings (preferred orientation, contrast 100%, size 15° by 60°, and spatial frequency 0.25–0.35 cycle per degree, cpd) were centered on the population receptive field and were presented at 8 different phases (0–315°, spaced at 45°) for 1.5 s. Typically 10 stimulus trials (for orientation and spatial frequency) or 20 stimulus trials (for visuotopy and phase) were presented along with blank stimulus trials (random order) with 2–5s inter-stimulus intervals.

Perfusion and Histology

At the end of the experiments, the animal received a lethal injection of Euthasol and was perfused transcardially with 0.9% saline, followed by 4% paraformaldehyde or 10% formalin. The brain was then removed, post-fixed in 4% paraformaldehyde or 10% formalin overnight, transferred to a 30% sucrose solution in phosphate buffer (PB, pH 6.8) and stored at 4°C for at least two days. The area of interest was blocked and then cut on a freezing microtome with 50 μm thick parasagittal, coronal or tangential sections collected in serial order. For immunostaining, the slices were incubated in blocking solution for 30 min, and then transferred to the primary antibody solution (chicken anti-GFP, 1:1000, Aves Labs, GFP-1020; rabbit anti-NeuN, 1:1000, Millipore, ABN78; guinea pig anti-vGlut2, 1:10000, Millipore, AB2251; mouse anti-PV, 1:1000, Swant; 235) for overnight incubation at 4°C. The slices were then incubated in secondary antibody (Alexa 405 for NeuN, 488 for GFP, 568 for vGlut2, 647 for PV; Invitrogen) for 2 hours at room temperature, mounted on glass slides, dried, and cover-slipped. Labeled neurons and structures were viewed on the fluorescence microscopy (Olympus BX53) or confocal microscope (Zeiss 710 Confocal, 20x objective). We verified all the injection and imaging sites were centered within 1 mm range from the center of the primary visual cortex, which processes the visual information covering –10~10 degree in elevation from the horizontal meridian and 0~20 degree in azimuth from the vertical meridian.

Data analysis

Mechanical drift in the imaging plane was corrected using customized motion registration program written in Matlab (Mathworks). Analyses were performed using custom code written in Matlab or Java package for running ImageJ within Matlab (Miji)[33]. The circular regions of interest (ROIs) corresponding to visually identified neurons were selected using ImageJ. ROIs were drawn by hand and selected by viewing the average intensity or standard deviation z-projection of the stack of two-photon images from one experiment, combined with visual examination of individual imaging frames. The fluorescence of each cell was measured by averaging all pixels within the ROI. Whenever we probed the feature selectivity of a column, we always first aligned and collapsed multiple cortical depths (at least three) from the same two-photon field of view into a 2D field of view for straightforward visualization.

Sparse noise receptive field measurement—Hand-mapping with a customized program written in Psychopy2[34] was used to determine the area of visual space relevant for the cortical field of view and to verify the stability of the population receptive field during

the experimental session. The sparse noise stimulus was then centered on the population receptive field center, ensuring that all of the neurons in the imaged area had receptive fields that fell within the stimulus presentation area. Linear receptive fields (RF) were obtained by reverse-correlating neuronal responses to an image set containing both white and black squares. The distribution of ON and OFF response regions were obtained by reverse correlation to image sets containing a single contrast polarity (either white or black respectively).

Reverse correlation analysis began by filtering the fluorescence signal from individual neurons (7 Hz low-pass zero-phase) and then applying a threshold at two standard deviations from the mean. Individual peaks in the trace were detected as fluorescence events, and the area under the curve of the rising phase was assigned to the peak time as a measure of the response strength for the corresponding fluorescence event[35]. The spatial temporal receptive field was reconstructed with repeating reverse correlation from 0–850 ms after stimulus onset in 50 ms time windows. The signal-to-noise ratio (SNR) for time τ was calculated as the ratio of the spatial variance between time τ and the stimulus onset time

$$\sigma_{xy}^2(\tau)/\sigma_{xy}^2(stimulus\ onset),\ \text{where}\ \sigma_{xy}^2(\tau) = \langle [R(x,y,\tau) - \langle R(x,y,\tau)\rangle]^2 \rangle_{x,y}.$$

The peak SNR for each neuron was obtained from a smooth spline fitting of the SNR curve. Receptive fields or individual ON/OFF response regions of neurons whose peak SNR values did not exceed 2.2 were not included in the analysis, thereby excluding spontaneously active, non-responsive cells. The receptive field was then resized to 48 by 48 pixels and the significance of each pixel was assessed by comparison with pixels from 100 randomly shuffled receptive fields (reverse correlation repeated 100 times for each neuron, using the time of the peak SNR). A significant pixel was defined as a pixel with an absolute value higher than the absolute value of the mean + 5 x standard deviation of the shuffled receptive field. Neurons whose receptive fields did not contain any significant pixels were excluded from further analysis. Fifty seven percent of the neurons that were imaged met both the signal to noise, and pixel statistical significance criteria, and were used for further analyses. In order to verify that our method for analyzing calcium signals did not impact the structure of the RFs, we selected the RFs with high SNR (>10) and computed the similarity index (SI)[17] of RFs derived from our original method with RFs derived with six alternative methods:

$$\frac{\sum_{x,y} RF_0(x,y) \cdot RF_1(x,y)}{\sqrt{\sum_{x,y} RF_0^2(x,y) \cdot RF_1^2(x,y)}},$$

where the RF_0 is the RF derived with the original method describing above, and RF_1 the RF derived with alternative methods. The alternative methods included RFs derived: (1) without applying a filter to the calcium trace; (2) without applying a threshold of two standard deviations ; (3) with the response strength of each event calculated as the area under the curve (AUC) of each peak of the fluorescence signal or (4) as AUC of the each peak of

fluorescence signal relative to the baseline fluorescence level; (5) with event time assigned to the initial deflection point of each fluorescence peak, (6) with event detection performed using a standard de-convolution method[36].

Neurons were placed into one of 3 classes: Simple, complex, and single sign (either ON or OFF). Forty-nine % of the neurons were found to have statistically significantly responses to only one sign of the sparse noise stimulus (either ON or OFF) and were categorized as single sign. Others with statistically significant responses to both dark and light sparse noise stimuli were further characterized as simple or complex cells based on the degree of segregation of the ON and OFF response fields. For this purpose we employed an ON/OFF segregation index

$$\mathrm{ON/OFF\ seg} = \frac{\sum_p |R'_{\mathrm{ON}}(p) - R'_{\mathrm{OFF}}(p)|}{\sum_p R'_{\mathrm{ON}}(p) + R'_{\mathrm{OFF}}(p)},$$

where $R'\mathrm{ON}(p)$ is all the pixels modulated by the light sparse noise stimulus and $R'\mathrm{OFF}(p)$ is all the pixels modulated by the dark sparse noise stimulus. Neurons with an ON/OFF segregation index greater than 0.6 were classified as simple cells while those with an index less than 0.6 were classified as complex cells[11]. For those neurons that responded significantly to both dark and light sparse noise stimuli, we also characterized the relative effectiveness of dark and light stimuli by calculating the ON/OFF ratio

$$\frac{\mathrm{ON}}{\mathrm{OFF}}\mathrm{ratio} = \frac{\max(SNR_{\mathrm{ON}})}{\max(SNR_{\mathrm{ON}}) + \max(SNR_{\mathrm{OFF}})}.$$

In order to evaluate the visuotopic organization of receptive field centers, and the centers of the ON and OFF subfields of simple cells, we calculated the center of mass of these regions in visual space using the absolute value of all the significant pixels in the receptive field or the subfield respectively. In a few cases where a simple cell had more than one significant ON or OFF subfield (%), only the subfield with the maximum (for ON) or minimum (for OFF) value was selected for estimating the neuron's subfield center of mass. Thus each simple cell could be summarized as having one receptive field center, one ON subfield center and one OFF subfield center.

To test if the offset between the ON and OFF subfields of simple cells could be used to estimate the cell's preferred orientation, the predicted orientation preference was defined as the orientation perpendicular to the axis of the receptive field dipole (a line connecting the ON and OFF centers). To test whether the phase tuning can be predicted from the simple cell receptive field structure, the receptive field was used as a 2D filter and convolved with a stimulus grating with eight phases to derive a predicted phase tuning curve, which was then fit with a Gaussian. This result was then compared with the experimental phase measurement data.

To characterize the feature selectivity of simple cells in a single orientation column, we first aligned and collapsed all the cortical depths (at least three) from the same two-photon field of view into a two dimensional neuron population. In order to sample from columns of cells with similar orientation preference, we employed an 80 μm diameter sample window and moved it in 5 um steps across the field of view, searching for sites that met the following criteria: more than 12 simple cells with a maximum orientation difference from the mean of the population less than 11.25 degrees and not containing more than 4 cells that were included in other columns. The values that we used to define an orientation column were based on the average bandwidth of the active zones produced in cortex by the presentation of a single grating stimulus. In cortical distance, the mean full width at half maximum was 86.7 ± 7.6 μm (N=106). On average, the range of orientation preferences exhibited by the neurons in this cortical area extended 11.9 ± 2.4 degrees beyond the orientation of the stimulus (HWHM). The aggregate receptive field (ARF) was then computed as the average of the normalized amplitude of all the simple cells within the orientation column. To estimate the predicted feature selectivity from the ARF, the ARF was fitted and parameterized with a two-dimensional Gabor function using the Levenberg–Marquardt algorithm[37]. The Gabor function is described by

$$G(x,y) = A\exp\left(-\frac{x'^2}{2\sigma_x^2} - \frac{y'^2}{2\sigma_y^2}\right)\cos(2\pi f x' + \varphi),$$

where (x', y') is obtained by translating the original coordinate system and rotating it by θ

$$x' = (x - c_x)\cos\theta - (y - c_y)\sin\theta$$
$$y' = (x - c_x)\sin\theta + (y - c_y)\cos\theta.$$

The Gabor function can be also viewed as an underlying two-dimensional cosine grating parameterized by θ (orientation), f (spatial frequency) and φ (relative spatial phase), which is enveloped by a two-dimensional Gaussian function parameterized by A (amplitude), c_x and c_y (centre of the Gaussian), and σ_x and σ_y (standard deviations of the Gaussian in perpendicular and parallel axis of the grating, respectively). All the fraction of explained variance from Gabor fits were at least 0.7. The aspect ratio of the Gabor fit was defined as σ_y/σ_x and the number of half-cycles within the Gaussian envelop was defined as $8f\sigma_x$. To assess the preference of the orientation column from the experimental tuning data, we used the average (or circular average for orientation and absolute spatial phase) of the preferences of all of the simple cells within the column. To evaluate the relation between orientation preference and the angle of ON subfield displacement, the ON-dipoles for the orientation column were determined by applying the k-means clustering (Matlab) to all the ON centers within the column with the assumption of two clusters. The predicted orientation preference for the column was defined as the orientation orthogonal to the axis of the ON-dipoles.

Tuning curve and preference map for multiple visual properties—For computing tuning properties, the fluorescence signal was calculated as F/F = (F-F0)/F0, where F0 is the baseline fluorescence signal averaged over a 1 s period immediately before the start of visual stimulation, and F is the fluorescence signal averaged over the first 1.5 s period after the start of the visual stimulation. For example, orientation tuning curves were obtained by calculating the mean fluorescence signal (F/F) for each orientation, and then fitting a Gaussian curve to the resulting data. Neurons were considered to be visually responsive if the maximum stimulus related fluorescence response (F/F) to any orientation was greater than 5% on average, and also greater than two standard deviations above the mean baseline fluorescence. In addition, we required that cells respond at least two standard deviations above baseline on at least 20% of the trials tested. Neurons were considered to be orientation tuned if they were visually responsive and also met the following criteria: 1) Well fit by the Gaussian function (r > 0.7, p < 0.05), and 2) Tuning index (TI) > 0.4

$$\mathrm{TI}=\frac{\mu_{\mathrm{pref}}-\mu_{\mathrm{ortho}}}{\mu_{\mathrm{pref}}+\mu_{\mathrm{ortho}}},$$

where μ_{pref} equals the mean response to the preferred orientation, μ_{ortho} equals mean response to the orthogonal orientation. For analysis of visuotopy and spatial frequency, a similar index was used but the response to the orthogonal stimulus was replaced by the response to a bar stimulus presented outside population receptive field or response to a grating with spatial frequency at 3.2 cpd, respectively. The preferred tuning properties and tuning width were calculated from the Gaussian curve fitting. For pixel based preference maps in both two-photon and epi-fluorescence imaging, we used data binned from areas of 10x10 pixels and assigned the preferred tuning value to each unit followed by smoothing with a 20 μm radius Gaussian filter.

To examine the relationship between the precision of the visuotopic arrangement of ON/OFF subfields and map structure, we computed the local heterogeneity for each cell in the orientation preference map. To obtain local heterogeneity we calculated the circular variance of the orientation tuning distribution of all of the pixels surrounding the cell, weighting the values obtained from each pixel using a Gaussian function with a σ of 30 μm and a cutoff at 50 μm:

$$\mathrm{Circular\ variance}=1-|\frac{\sum_k r_k \exp(i2q_k)}{\sum_k r_k}|,$$

Where r_k is the magnitude of the responses (F/F) to the stimulus k with orientation θ_k.

To evaluate the extent of cortical activity evoked by a single bright (ON) or dark (OFF) bar with epi-fluorescence imaging, the F/F of each pixel in the area of activation was calculated. The width of the activated region was estimated by averaging the response along the visuotopic axis orthogonal to the orientation of the bar stimulus. The half width at half maximum (HWHM) was computed for each visual stimulus, by using stimulus positions in which both the ON and OFF evoked responses were centered within the imaging window.

To evaluate the distribution in visual space of the ON and OFF subfields of simple cell populations, we calculated the pairwise distance between the centers of individual subfields for all ON centers, all OFF centers, all centers with the same signs, and all centers with different signs. These values were compared to the pairwise distances derived from the random shuffling of sign identity in 10 independent repetitions. A similar analysis was preformed for RF centers by comparing the pairwise distance of the original RF centers to the pairwise distances created by shuffling the angle in polar coordinates, but keeping the radian from the population center the same, in 10 independent repetitions. For each imaging area, the pattern of the distribution for any relationship can be summarized as the log ratio between the mean pairwise distance from data and shuffle: negative value indicated more clustered than by random chance, while positive value means more scattered than by random chance.

The cellular precision of fine visuotopy was tested for the RF centers and the centers of OFF and ON subfields from the same population of neurons. Elevation and azimuth coordinates were used to evaluate visuotopic precision in each dimension. To quantify deviations from smooth visuotopy, Pearson's correlation coefficients were applied to each visuotopic center position and their distance along the cortical representation for each visuotopic axis. For each field of view, the average deviation from a smooth visuotopy and the goodness of fit were used as a measure of precision in visuotopy.

The precision of mapping for absolute spatial phase was tested at the cellular level with two-photon imaging and over a larger scale with epi-fluorescence imaging. Because absolute spatial phase maps are defined with a static gratings of the same orientation and the full range of phases, we calculated the smoothness of the phase map by limiting analysis to regions of cortex responsive to the testing orientation. To define the single orientation responsive region (SORG) for constraining the phase map, orientation contour lines were drawn for the specific testing orientation plus and minus 30° on the filtered orientation preference map. This is based on the average size of the responsive area evoked by flashing a static grating stimulus with a single orientation under two-photon imaging. Neurons or pixels falling within the orientation preference contour lines of SORG were then selected for the further analysis. We generated a theoretic prediction of a smooth phase map by projecting the 2D phase map along the orthogonal axis of visuotopy and applied a linear fit to each 360° periodic cycle. The one dimensional phase gradient was then transformed into a two dimensional phase map with interpolation. The phase preference of individual cells from two-photon imaging or that of individual pixels in epi-fluorescence imaging was then correlated to the prediction from the smooth phase map. To measure the intersection angle between maps[38], the vector indicating the change of the preferred feature was extracted for each pixel, and the angular difference of all the pixels within the region of interest was compared for different functional maps. To characterize the statistical structure of functional maps, we compared the relationship between cortical distance and the mean of preferred feature. The cortical distance shorter than the first meet between the real and shuffled data was defined as the clustering effect of the preferred feature. The periodicity of the map was computed by sinusoidal fit to the data points beyond the distance of feature clustering.

General statistics

Statistical analyses were performed in Matlab. We used two-sided non-parametric Wilcoxon rank-sum test to compare two groups and Kruskal-Wallis test to compare multiple groups with *post hoc* tests using Dunn's test, without assumptions of normality or equal variances. Circular correlation coefficient was used for orientation and spatial phase, while Pearson's correlation coefficient was applied to visuotopy and spatial frequency. Rayleigh test was used to test the uniformity of the intersection angle distribution between the two maps. All statistical methods are two-sided. No estimates of statistical power were performed prior to experiments.

V1 computational model

In order to evaluate the uniformity and completeness of coverage for orientation and absolute spatial phase, we began by simulating the underlying receptive field structures from the large-scale functional maps. We used the orientation map derived from intrinsic signal imaging in the tree shrew[39] and the phase map, generated using published data on visuotopy and cortical magnification factor[5, 10]. We then generated a Gabor-like simple cell receptive field for each pixel, using the typical scale for single cortical neurons. The ON/OFF subfield organization for each pixel was then modeled using the relationships described in the results of this study: i.e., the center of OFF subfields of the cortical population followed a perfect visuotopic map, distributed according to the cortical magnification factor, while the center of ON subfields followed an orientation specific displacement for the simple cell, randomly placed on either side of the OFF center with a distance of 3.5° visual angle.

We used the receptive field derived from each pixel in the functional map as a spatial filter for visual stimulation. A theoretical cortical response was derived using a circular patch stimulus with both negative and positive contrast, varying in both size and visual location. The output of the cortical activity pattern was then transformed into a luminance scale overlaid on the functional map for visualizing the area and functional properties that were covered. We defined δ as the distribution of the functional properties covered within the responsive area divided into eight bins for either orientation or spatial phase, and then evaluated the coverage from these distributions in several ways[5,40]: First, the completeness of coverage was calculated as the number of bins with a positive number divided by total numbers of bins. Second, the uniformity of coverage (c') was computed using the following equation:

$$c' = \frac{\text{standard deviation}(\delta)}{\text{mean}(\delta)}$$

Uniformity of coverage was computed in two ways: (1) using the original counts of the pixels within the responsive area, and (2) weighting the properties of the pixels by their responsive strength. The coverage for phase was always calculated independently for each orientation and then averaged. Overall, a lower c' value indicates greater uniformity of coverage.
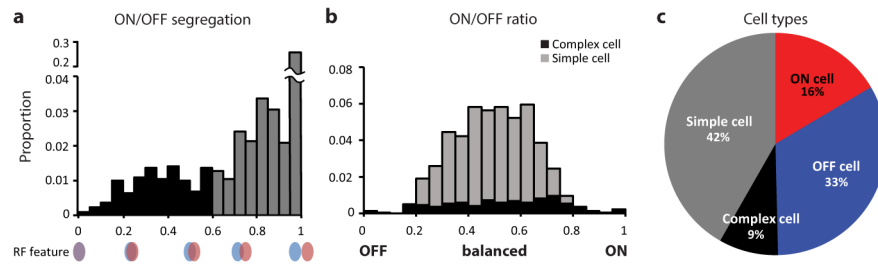
Extended Data
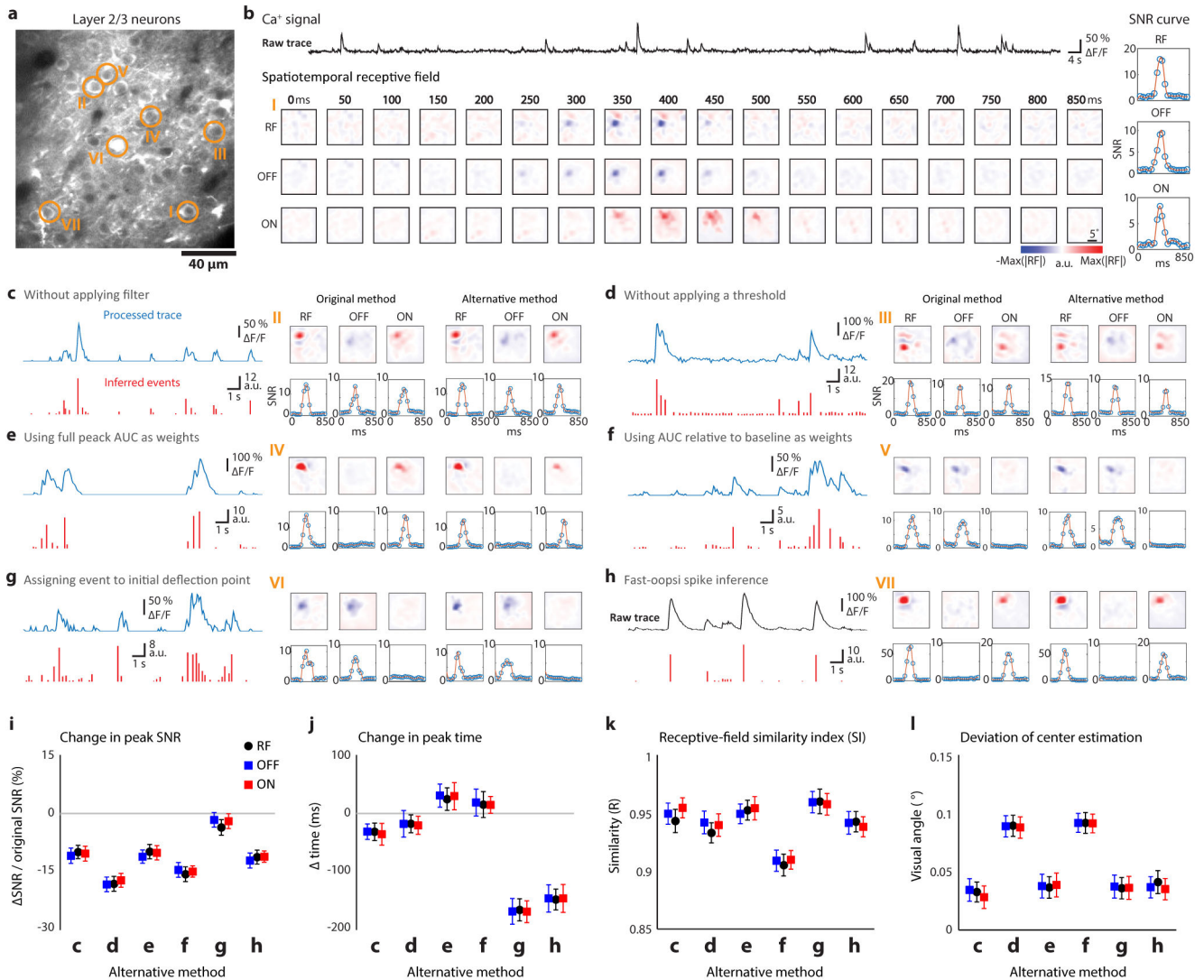
Extended Data Figure 1. Robust receptive field estimation from GCaMP6 calcium signal in layer 2/3 neurons

**a,** Somatic location of seven example cells (circle) overlaid on the two-photon field of view. **b**, Raw calcium trace, spatiotemporal receptive field and signal-noise ratio (SNR) curve from an example cell in **a. c–h,** Six different ways to infer the onset time and response strength of neural activity were used to compare with the original method described in Methods for six example cells in **a**. Processed calcium trace before starting inference (blue) and the inferred response (red) are shown on the left. Receptive fields/SNR curves derived from original or alternative method are shown on the right. **i–l,** Change in peak SNR (i) and peak time (j), receptive field similarity index (k), deviation of the RF/subfields center estimation (l) illustrating that the main conclusions regarding receptive field structure and fine visuotopic organization are not altered by the signal processing method employed (N = 143 cells from 3 animals). All error bars indicate s.e.m.

Extended Data Figure 2. Cell type categorization in tree shrew primary visual cortex layer 2/3
a, Distribution of ON/OFF segregation index values for simple and complex cells (see Methods). A value of 0.6 was used to delineate the two classes. **b,** Distribution of ON/OFF ratio values for simple and complex cells. In both **a** and **b**, the proportions are based on the total number of cells; however, the single sign cell population is not shown in the plots. **c,** Percentage of different classes of neurons in tree shrew visual cortex layer 2/3.
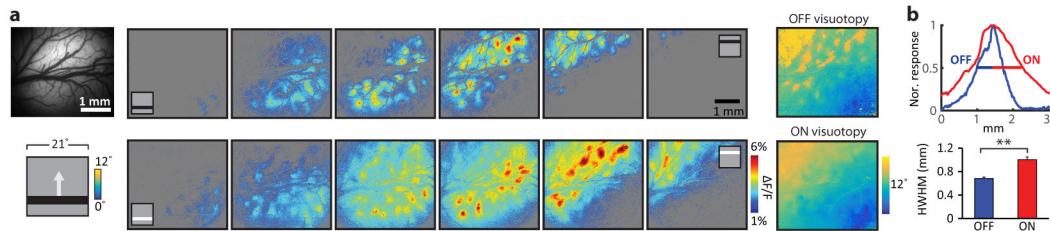
Extended Data Figure 3. Cortical spread of light and dark evoked activity in epi-fluorescence imaging
a, The wide field epi-fluorescence imaging of visual cortex reveals a similar visuotopic progression for the zones of activity found for static light and dark bar stimuli at different locations in elevation. **b,** The bandwidth of the normalized cortical activity pattern, characterized by half width at half maximum (HWHM), shows that the light stimuli evoke broader cortical activity patterns than dark stimuli at the same visuotopic location (N = 21 stimulus-evoked response maps from 4 animals, $P = 9.6 \times 10^{-5}$, rank-sum test). Error bars indicate s.e.m.
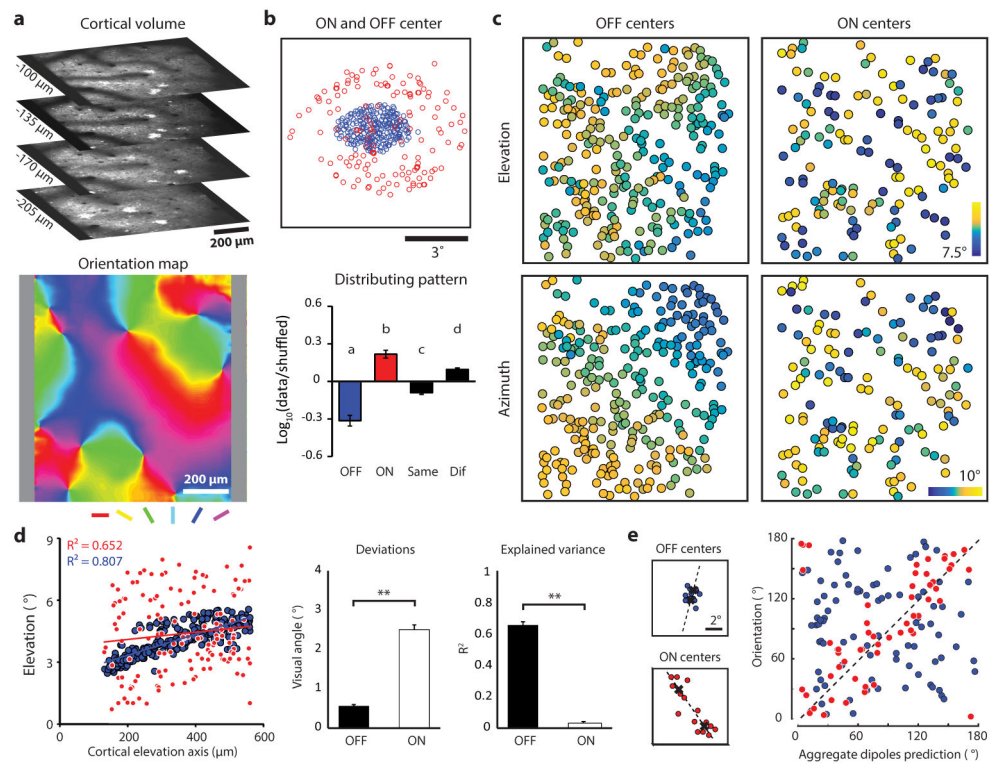
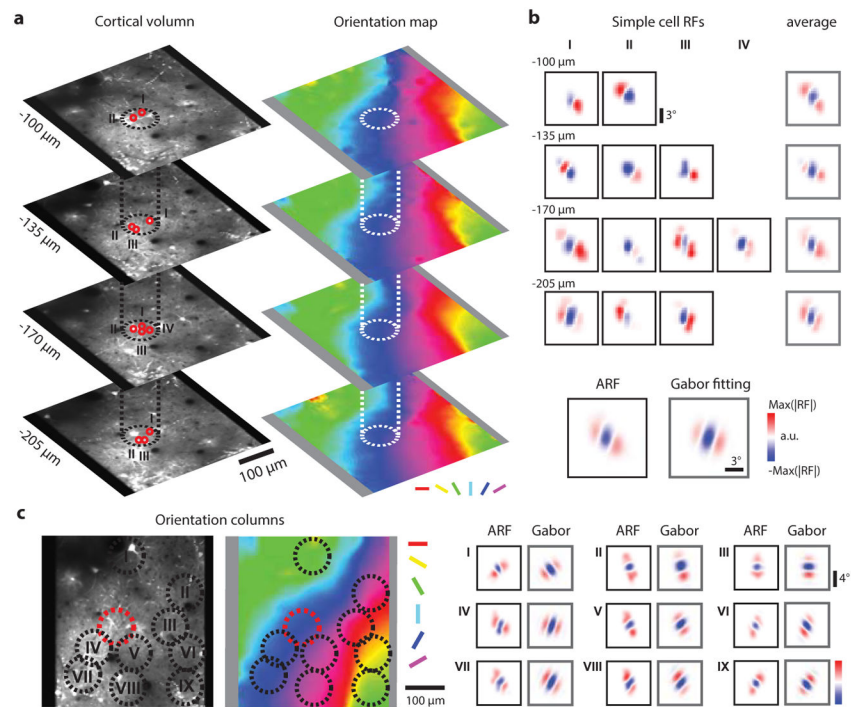**Extended Data Figure 4. ON and OFF receptive field organization of single sign cells**
a, The cortical volume and the orientation map of an example imaging area. **b,** The ON and OFF centers from single sign cells display an arrangement similar to the simple cell population. The bottom plot shows that the distribution pattern of ON and OFF receptive fields is consistent with the ON- and OFF- subfields of the simple cell population (N = 8 imaging areas from 7 animals, Kruskal-Wallis test; compare with Fig 1c and d, letters indicating groups with statistically significant difference, P < 0.01). **c,** The visuotopic organization of ON and OFF receptive field centers was similar to the simple cell ON- and OFF- subfields. **d,** The relation between cortical distance and visuotopic position demonstrating the difference in visuotopic precision for ON and OFF receptive fields (linear regression). Deviations of the experimental results from the linear fit and explained variance of the smooth visuotopy (N = 16 visuotopic maps, combining elevation and azimuth results from 8 imaging areas, **p < 0.0001, rank-sum test) are consistent with the results from simple cell ON- and OFF subfields. **e,** Only the displacement of the population ON receptive field center, but not OFF receptive field center, can predict the orientation tuning of the orientation column (circular correlation, N = 68 cortical columns, P = 9.51×10^{-3} for ON; N = 89 cortical columns, P = 0.586 for OFF). All error bars indicate s.e.m.
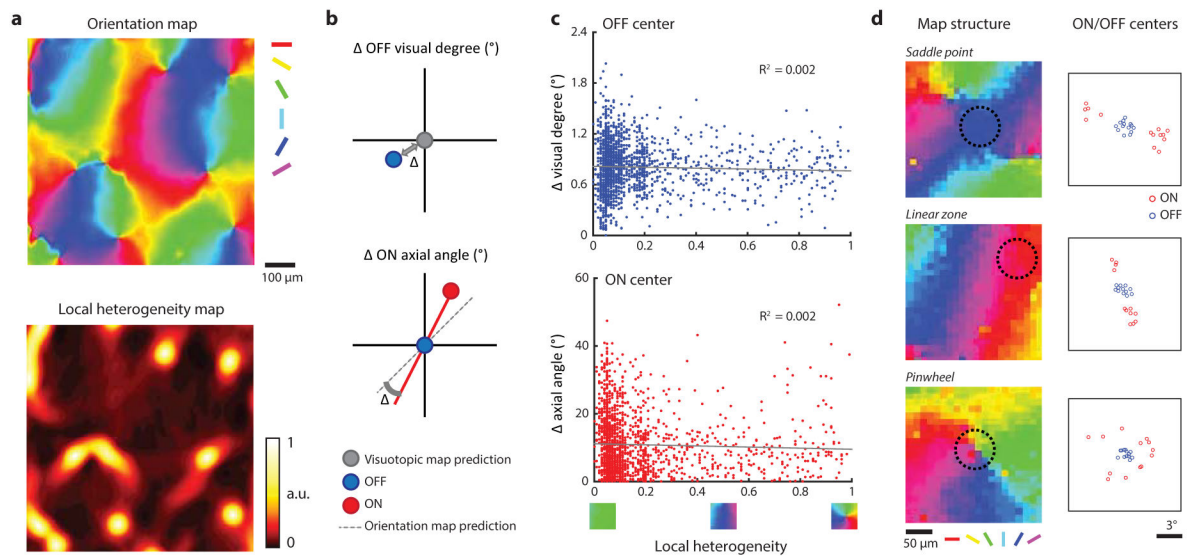
Extended Data Figure 5. Visuotopic arrangement of ON and OFF subfields is independent of orientation map structure

a, An example orientation map and local heterogeneity index map. The local heterogeneity index was used to compare ON and OFF subfield arrangement for cortical regions with different orientation map structure. **b,** (top) Illustration comparing the visuotopic displacement of OFF subfields to the theoretical prediction from a smooth visuotopic map. (bottom) Illustration comparing the visuotopic displacement of ON subfields to the orientation map. **c,** (top) Visuotopic distortion of OFF subfield centers in relation to the structure of the orientation map. There is no relationship between local heterogeneity and the visuotopic precision of OFF subfields (linear regression, N = 1811 cells from 7 animals, P = 8.2×10^{-2}). (bottom) Axial mismatch of ON subfield centers in relation to the structure of the orientation map. There is no relationship between local heterogeneity and the axial displacement of ON subfield centers (linear regression, N = 1811 cells, P = 9.6×10^{-2}). **d,** Examples of the ON and OFF subfield center distributions from an 80 μm circular region (black circle) centered on three distinct regions of orientation map.

Extended Data Figure 6. Contribution of simple cells at different depths to aggregate receptive field of cortical column

a, An example orientation column at four depths, with two-photon images on the left and the corresponding orientation maps on the right. **b,** Simple cell receptive fields from these four cortical depths. Each RF was normalized by the strongest subfield. The average of the RFs within each depth appear similar. All the RFs within the orientation column were then pooled into an aggregate receptive field (ARF) and then fitted with 2D Gabor function. **c,** Other nine examples of ARFs from different orientation columns display the same organization: OFF subfield in the center with ON subfields flanking on two sides.
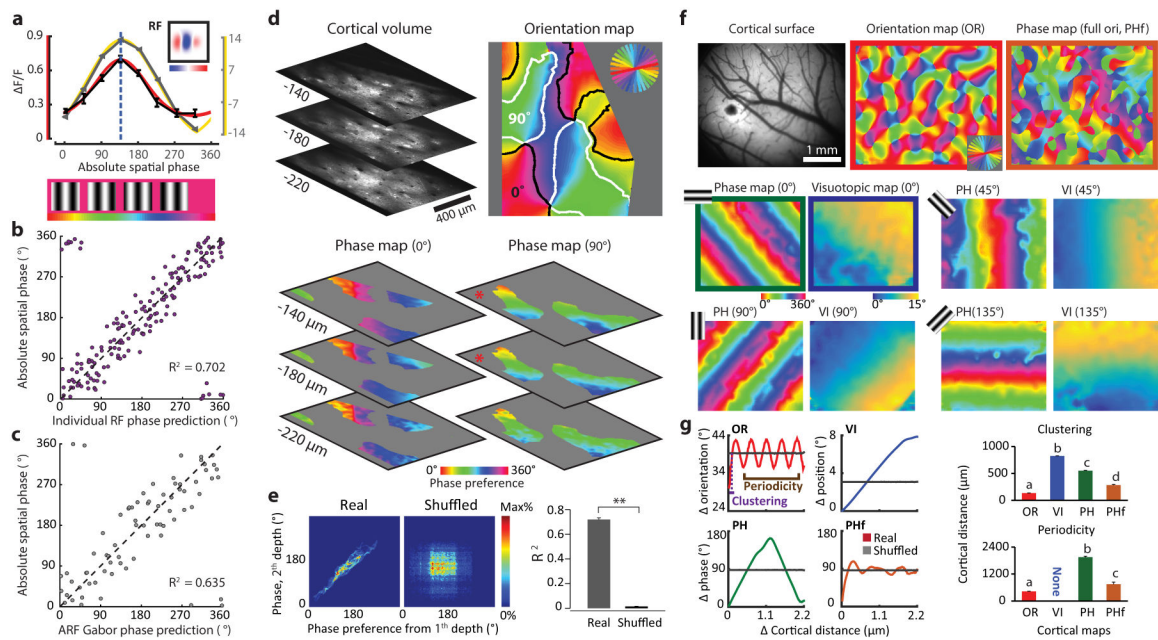
Extended Data Figure 7. Characterizing spatial phase tuning, phase column, and phase map
a, The phase tuning from an example cell (black) and its Gaussian fit (red) compared with the phase tuning curve predicted from its receptive field structure (gray) and its Gaussian fit (yellow). Dashed line depicts the preferred phase derived from the Gaussian fit to the experimental data. **b,** Relation of absolute phase prediction from receptive field structure to absolute phase tuning measurement (N = 179 cells from 2 animals, P = 1.8×10^{-18}, circular regression). **c,** Phase preference of the orientation column is well predicted by the phase parameter of the Gabor fit to the ARF (N = 73 cortical columns from 5 animals, P = 1.7×10^{-10}, circular regression). **d,** Example two-photon phase maps derived from pixel tuning at three cortical depths for both horizontal and vertical orientations. **e,** Comparison of phase preference from different cortical depths (red asterisks in **d**) showing the consistence of columnar structure for spatial phase (rank-sum test for R^2 from circular regression, N = 36 pairs of maps at different depths from 2 animals, P = 8.2×10^{-18}). **f,** Large scale functional maps visualized by epi-fluorescence imaging. The phase map with full orientation coverage (right) was constructed from four individual phase maps measured independently with four orientations (0°, 45°, 90°, 135°). The phase maps for single orientations with corresponding visuotopic maps are shown separately in lower two rows. **g,** The statistical structure of functional maps (orientation, phase, visuotopy, and phase with 4 orientations) summarized by the relationship between the change in cortical distance and the average change in preferred feature (left). Summary comparison of clustering and periodicity of the preferred features of four functional maps from 6 animals (right). Each map exhibits distinct clustering and periodicity (N = 32 sample regions from 6 animals, Kruskal-Wallis test with *post hoc* using Dunn's method, letters indicating groups with statistically significant difference, P < 0.05). All error bars indicate s.e.m.
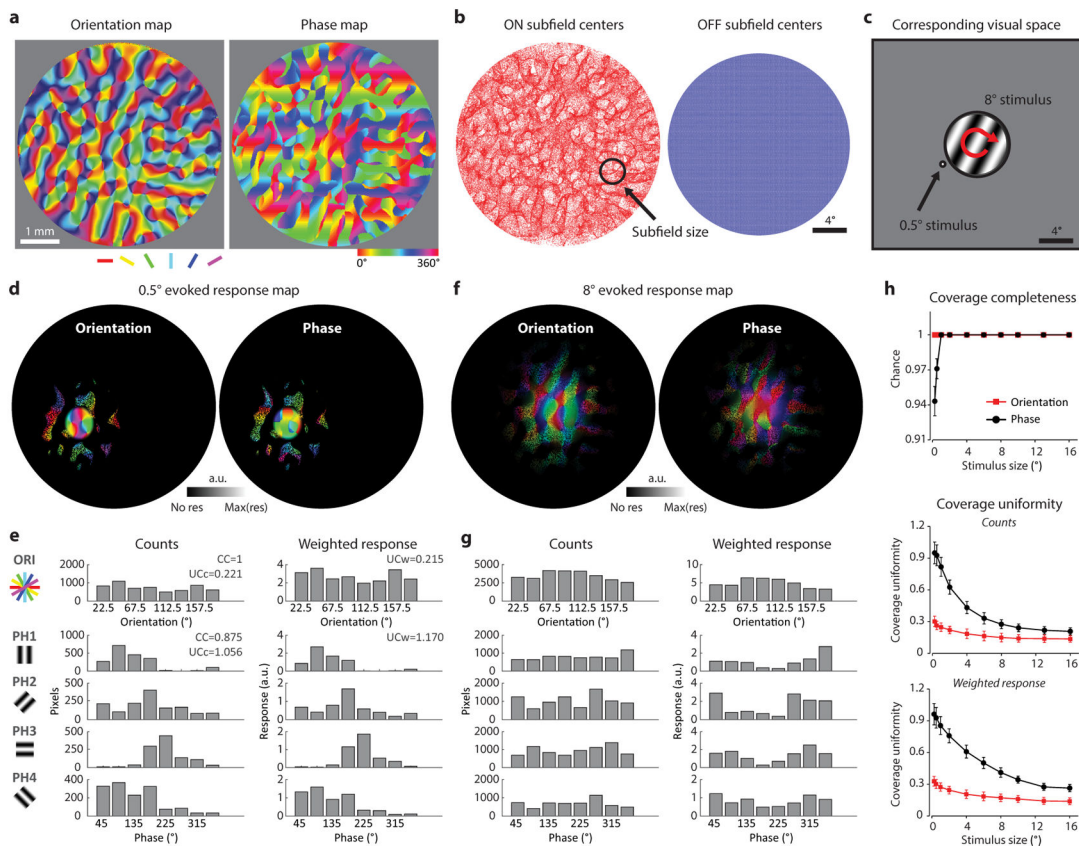
Extended Data Figure 8. Simulation based on experimental observations to evaluate completeness and uniformity of coverage for orientation and phase representations
a, The large scale orientation preference map derived from intrinsic signal imaging and corresponding phase map predicted from experimental observations (see Methods). **b,** Distribution of ON and OFF subfield centers in visual space predicted from the visuotopic precision and orientation specific displacement demonstrated in this study. Although the distribution of the ON subfield centers in visual space appears uneven, complete coverage of visual space is achieved when the actual size of the ON subfields is considered. **c,** Illustration of two of the visual stimuli (8 degree stimulus in the center, 0.5 degree stimulus to the left) used to simulate the evoked response map. **d,** Theoretical stimulus evoked orientation and phase response maps for sample 0.5° stimulus shown in **c** (see Methods). **e,** Histograms showing the distribution of preferred orientation and phase values for pixels activated in **d**, calculated by counts of the pixels in the responsive region (left) or weighted by the strength of the responses (right). **f,** Theoretical stimulus evoked orientation and phase response maps for sample 8° stimulus shown in **c** (see Methods). **g,** Histograms showing the distribution of preferred orientation and phase values for pixels activated in **f**, calculated by counts of the pixels in the responsive region (left) or weighted by the strength of the responses (right). **h,** Completeness (top) and uniformity (middle, bottom) of coverage simulated with visual stimuli of various sizes and positions. Complete coverage can be achieved with stimuli of 1 degree, while coverage uniformity continues to improve with increases in stimulus size. The results of spatial phase were always the average results obtained with four different orientations. Error bars indicate s.e.m.

Supplementary Material

Refer to Web version on PubMed Central for supplementary material.

Acknowledgments

References

1. Hubel DH, Wiesel TN. Receptive fields, binocular interaction and functional architecture in the cat's visual cortex. J Physiol (Lond). 1962; 160:106–154. [PubMed: 14449617]

2. Ferster D, Chung S, Wheat H. Orientation selectivity of thalamic input to simple cells of cat visual cortex. Nature. 1996; 380:249–252. [PubMed: 8637573]

3. Jin JZ, et al. On and off domains of geniculate afferents in cat primary visual cortex. Nat Neurosci. 2008; 11:88–94. [PubMed: 18084287]

4. Jin J, Wang Y, Swadlow HA, Alonso JM. Population receptive fields of ON and OFF thalamic inputs to an orientation column in visual cortex. Nat Neurosci. 2011; 14:232–238. [PubMed: 21217765]

5. Bosking WH, Crowley JC, Fitzpatrick D. Spatial coding of position and orientation in primary visual cortex. Nat Neurosci. 2002; 5:874–882. [PubMed: 12195429]

6. Reid RC, Alonso JM. Specificity of monosynaptic connections from thalamus to visual cortex. Nature. 1995; 378:281–284. [PubMed: 7477347]

7. Alonso JM, Usrey WM, Reid RC. Rules of connectivity between geniculate cells and simple cells in cat primary visual cortex. J Neurosci. 2001; 21:4002–4015. [PubMed: 11356887]

8. Fan Y, et al. Genome of the Chinese tree shrew. Nat Commun. 2013; 4:1426. [PubMed: 23385571]

9. Rockland KS, Lund JS. Widespread periodic intrinsic connections in tree shrew visual cortex (Area 17). Science. 1982; 215:1532–1534. [PubMed: 7063863]

10. Bosking WH, Zhang Y, Schofield B, Fitzpatrick D. Orientation selectivity and the arrangement of horizontal connections in tree shrew striate cortex. J Neurosci. 1997; 17:2112–2127. [PubMed: 9045738]

11. Van Hooser SD, et al. Transformation of receptive field properties from lateral geniculate nucleus to superficial V1 in the tree shrew. J Neurosci. 2013; 33:11494–11505. [PubMed: 23843520]

12. Kretz R, Rager G, Norton TT. Laminar organization of ON and OFF regions and ocular dominance in the striate cortex of the tree shrew (Tupaia belangeri). J Comp Neurol. 1986; 251:135–145. [PubMed: 3760256]

13. Muly EC, Fitzpatrick D. The morphological basis for binocular and ON/OFF convergence in tree shrew striate cortex. J Neurosci. 1992; 12:1319–1334. [PubMed: 1313492]

14. Jones JP, Palmer LA. The two-dimensional spatial structure of simple receptive fields in cat striate cortex. J Neurophysiol. 1987; 58:1187–1211. [PubMed: 3437330]

15. Lampl I, Anderson JS, Gillespie DC, Ferster D. Prediction of orientation selectivity from receptive field architecture in simple cells of cat visual cortex. Neuron. 2001; 30:263–274. [PubMed: 11343660]

16. Ringach DL. Spatial structure and symmetry of simple-cell receptive fields in macaque primary visual cortex. J Neurophysiol. 2002; 88:455–463. [PubMed: 12091567]

17. Yeh CI, Xing D, Williams PE, Shapley RM. Stimulus ensemble and cortical layer determine V1 spatial receptive fields. Proc Natl Acad Sci USA. 2009; 106:14652–14657. [PubMed: 19706551]

18. Chichilnisky EJ, Kalmar RS. Functional asymmetries in ON and OFF ganglion cells of primate retina. J Neurosci. 2002; 22:2737–2747. [PubMed: 11923439]

19. Devries SH, Baylor DA. Mosaic arrangement of ganglion cell receptive fields in rabbit retina. J Neurophysiol. 1997; 78:2048–2060. [PubMed: 9325372]

20. Ratliff CP, Borghuis BG, Kao YH, Sterling P, Balasubramanian V. Retina is structured to process an excess of darkness in natural scenes. Proc Natl Acad Sci USA. 2010; 107:17368–17373. [PubMed: 20855627]

21. Miller KD. A model for the development of simple cell receptive fields and the ordered arrangement of orientation columns through activity-dependent competition between ON- and OFF-center inputs. J Neurosci. 1994; 14:409–441. [PubMed: 8283248]

22. Ringach DL. Haphazard wiring of simple receptive fields and orientation columns in visual cortex. J Neurophysiol. 2004; 92:468–476. [PubMed: 14999045]

23. Oppenheim AV, Lim JS. The importance of phase in signals. Proc IEEE. 1981; 69:529–541.

24. Pollen DA, Ronner SF. Phase relationships between adjacent simple cells in the visual cortex. Science. 1981; 212:1409–1411. [PubMed: 7233231]

25. Adelson EH, Bergen JR. Spatiotemporal energy models for the perception of motion. J Opt Soc Am A. 1985; 2:284–299. [PubMed: 3973762]

26. Kara P, Boyd JD. A micro-architecture for binocular disparity and ocular dominance in visual cortex. Nature. 2009; 458:627–631. [PubMed: 19158677]

27. Smith G, Whitney DE, Fitzpatrick D. Modular Representation of Luminance Polarity in the Superficial Layers of Primary Visual Cortex. Neuron. 2015; 88:805–818. [PubMed: 26590348]

28. Wang Y, et al. Columnar organization of spatial phase in visual cortex. Nat Neurosci. 2015; 8:97–103.

29. Smith SL, Häusser M. Parallel processing of visual space by neighboring neurons in mouse visual cortex. Nat Neurosci. 2010; 13:1144–1149. [PubMed: 20711183]

30. Cossell L, et al. Functional organization of excitatory synaptic strength in primary visual cortex. Nature. 2015; 518:399–403. [PubMed: 25652823]

31. Chen TW, et al. Ultrasensitive fluorescent proteins for imaging neuronal activity. Nature. 2013; 499:295–300. [PubMed: 23868258]

32. Pologruto TA, Sabatini BL, Svoboda K. ScanImage: flexible software for operating laser scanning microscopes. Biomedical engineering online. 2003; 2:13. [PubMed: 12801419]

33. Sage, D., Prodanov, D., Tinevez, JY., Schindelin, J. MIJ: Making Interoperability Between ImageJ and Matlab Possible. ImageJ User & Developer Conference; 24–26 October 2012; Luxembourg.

34. Peirce JW. PsychoPy–Psychophysics software in Python. J Neurosci Meth. 2007; 162:8–13.

35. Seelig JD, Jayaraman V. Feature detection and orientation tuning in the Drosophila central complex. Nature. 2013; 503:262–266. [PubMed: 24107996]

36. Vogelstein JT, et al. Fast nonnegative deconvolution for spike train inference from population calcium imaging. J Neurophysiol. 2010; 104:3691–3704. [PubMed: 20554834]

37. Jones JP, Palmer LA. An evaluation of the two-dimensional Gabor filter model of simple receptive fields in cat striate cortex. J Neurophysiol. 1987; 58:1233–1258. [PubMed: 3437332]

38. Nauhaus I, et al. Orthogonal micro-organization of orientation and spatial frequency in primate primary visual cortex. Nat Neurosci. 2012; 15:1683–1690. [PubMed: 23143516]

39. Huang X, et al. Optogenetic assessment of horizontal interactions in primary visual cortex. J Neurosci. 2014; 34:4976–4990. [PubMed: 24695715]

40. Swindale NV, Shoham D, Grinvald A, Bonhoeffer T, Hubener M. Visual cortex maps are optimized for uniform coverage. Nat Neurosci. 2000; 3:822–826. [PubMed: 10903576]
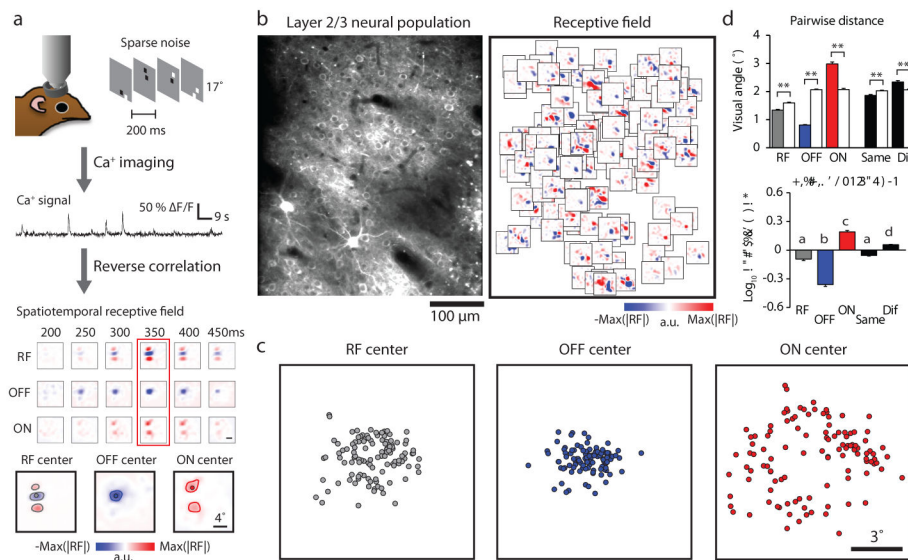
Figure 1. Differential arrangement of simple cell ON and OFF subfields in visual space
a, Spatiotemporal receptive fields and ON/OFF subfields of cortical neurons were independently obtained using calcium imaging combined with reverse correlation to a sparse noise stimulus. The receptive field and ON/OFF subfields were defined at the peak SNR time window. Small circles indicate the centers of mass of the whole RF and the ON/OFF subfields (see Methods). **b,** An example of a two-photon field of view and all the significant receptive fields (same scale as receptive fields in **a**) from individual cells overlaid on their soma locations. **c,** An example of the distribution of RF and OFF/ON subfield centers in visual space. **d,** The pairwise distance between the centers of mass for all categories and for shuffled data (white bars) from the example in **c**. Receptive fields, OFF subfields, and subfields sharing the same signs are more clustered while ON subfields and subfields with different signs are more scattered than by chance (rank-sum test for each group, **p < 0.0001). The bottom plot summarizes the comparison of real and shuffled data where positive values indicate a scattered distribution pattern and negative values indicate clustered distribution pattern relative to random shuffles (N = 8 fields of view from 7 animals, P = 6.1 5 10^{-21}, Kruskal-Wallis test with *post hoc* using Dunn's method; letters indicating groups with statistically significant difference, P < 0.01, see Methods). Error bars indicate s.e.m.
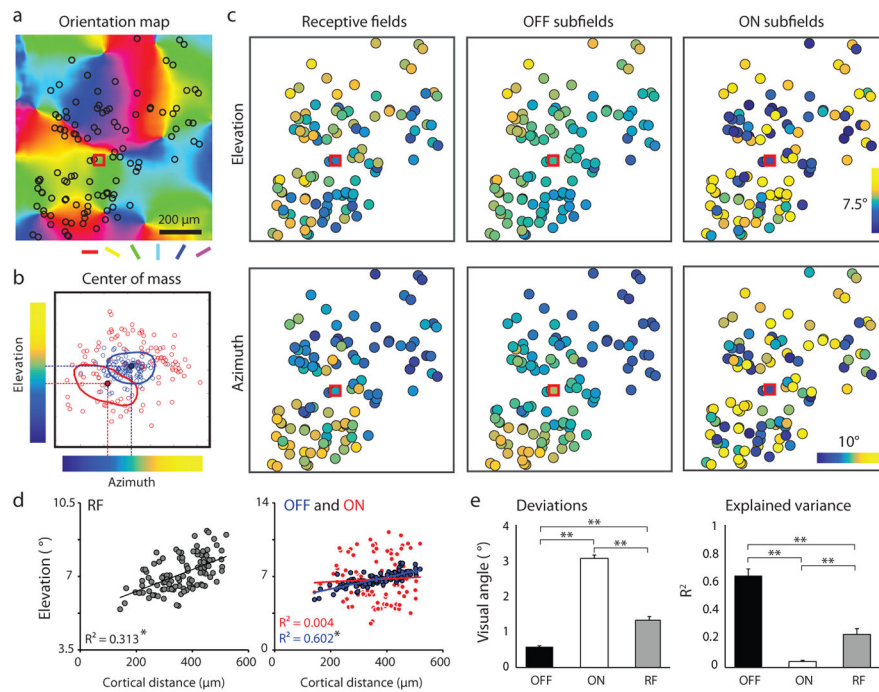
Figure 2. Differences in visuotopic precision of simple cell ON and OFF subfield centers
a, Example field of view showing somatic location of all simple cells from four cortical depths (black circles) superimposed on the orientation map. **b,** The location in visual space of the center of mass of ON and OFF subfields for neurons in **a** illustrating the color code that is used to depict azimuth and elevation values in **c**. RF of an example cell (red square in **a** and **c**) showing translation of ON and OFF subfield centers into elevation-azimuth coordinates. **c,** The visual field location (elevation and azimuth) for the receptive field and ON/OFF subfields for each neuron illustrated in **a. d,** The relation between cortical distance (along the elevation axis) and elevation in visual space for the receptive fields (left) and the ON and OFF subfields (right) from the example in **c**. (linear regression, *P < 0.0001). **e,** The summary showing the deviations of the experimental data from smooth visuotopy (left) and the degree to which a smooth visuotopy accounts for the variance in the experimental data (right) (Kruskal-Wallis test with *post hoc* using Dunn's method, N = 16 visuotopic maps, combining elevation and azimuth results from 8 imaging areas, **P < 0.0001; see Methods). Error bars indicate s.e.m.
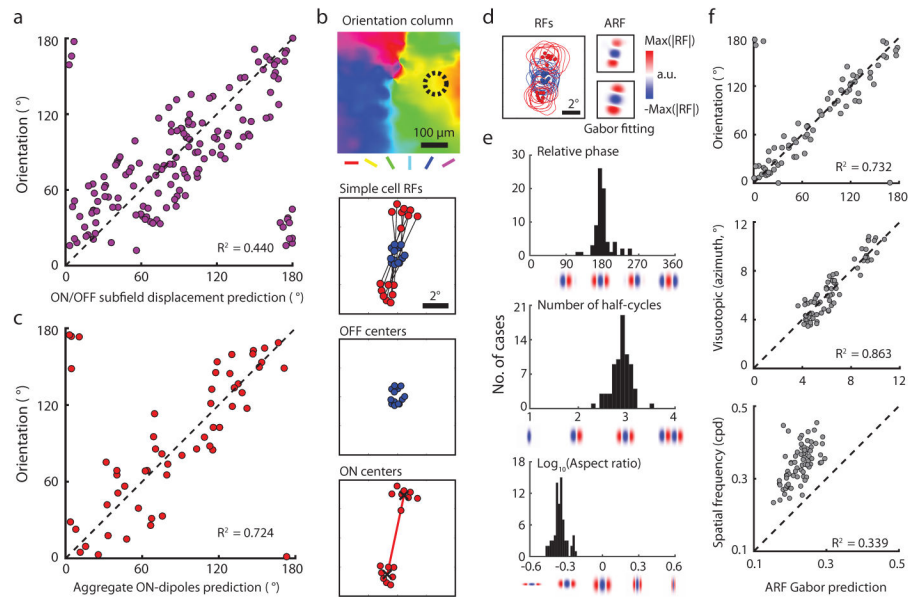
Figure 3. Orientation columns exhibit an invariant aggregate receptive field structure
a, Consistent with simple cells in other mammals, the ON/OFF subfield displacement in visual space predicts the preferred orientation in individual cells (linear regression, N = 176 cells from 2 animals, P < 0.0001). **b,** Example of receptive fields from the simple cells in a single orientation column (dashed circle). Lines connect the ON subfield (red) and the OFF subfield (blue) centers of individual simple cell receptive fields. The ON centers form two clusters that define the aggregate ON-dipole of the column. **c,** The aggregate ON- dipoles from all the simple cells within individual orientation columns predicts the preferred orientation of the column (linear regression, P < 0.0001). **d,** The normalized simple cell receptive fields from a single column in **b** were averaged to derive the aggregate receptive field (ARF) which was fit with a Gabor. **e,** Cortical columns exhibit an invariant ARF structure resembling an OFF centered simple cell receptive field with specific relative phase, number of half-cycles, and aspect ratio. **f,** The parameters of the ARF Gabor fit account for multiple features of the cortical column including orientation, visual position, and spatial frequency (N = 73 cortical columns from 5 animals, circular or linear regression, all P < 0.0001; see Methods).
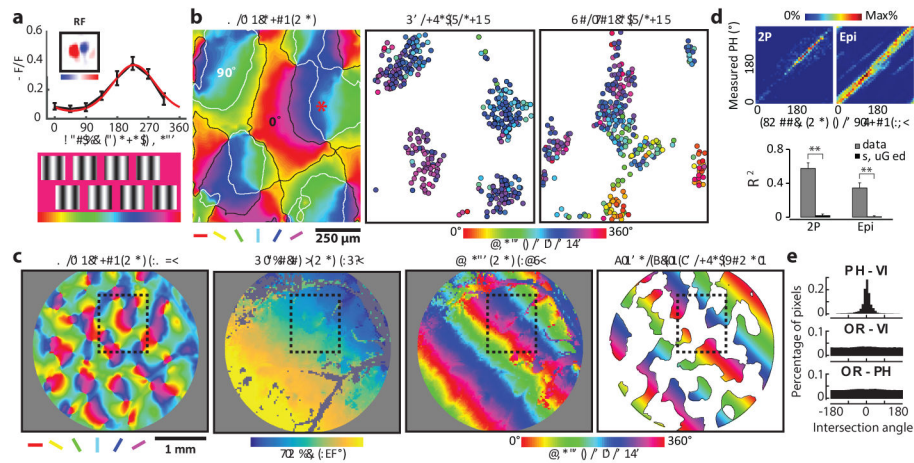
Figure 4. Smooth progression of absolute spatial phase across orientation domains
a, The phase tuning curve (black) and its Gaussian fit (red) for an example neuron derived from 8 static grating stimuli. **b,** Organization of the phase preference for populations of neurons derived with vertical and horizontal grating stimuli visualized with two-photon imaging at three cortical depths. Cortical domains with a significant response to vertical and horizontal gratings are delineated by contours (white and black respectively). Neighboring neurons exhibit similar phase preferences, and the preferences shift in a progressive fashion across the orientation domains. **c,** Epi-fluorescence imaging demonstrates relation of phase map derived with vertical grating to maps of orientation and visual space (azimuth). Black rectangle indicates the 2-P field of view shown in **b**. The smooth progression of preferred phase along the visuotopic axis orthogonal to the stimulus orientation is evident at this scale. The rightmost figure shows a linear fit of the phase signal within vertical orientation domains to approximate the phase preference map. **d,** Both for the two-photon and epi-fluorescence data, a smooth phase progression generated with a linear fit was used to test for correlation with the experimental data (circular regression, both P < 0.0001). The smooth progression accounted for a greater amount of the variance in the experimental data compared to shuffled data (**p < 0.0001, rank-sum test within group; see Methods). Error bars indicate s.e.m. **e,** The intersection of the phase and visuotopic map gradients shown in **c** peaks around 0 degree (0.32° in this case and −0.08° on average of six maps), indicating a parallel relationship (P = 5.2×10^{-16}, Rayleigh test), while there is no significant non-uniformity for the intersection of orientation map gradients with either phase or visuotopic map gradients (P > 0.05, Rayleigh test).